Correlating Symmetries of Low-Frequency Vibrations and Self-Trapped Excitons in Layered Perovskites for Light Emission with Different Colors

Miao-Ling Lin, Balaji Dhanabalan, Giulia Biffi, Yu-Chen Leng, Seda Kutkan, Milena P. Arciniegas,* Ping-Heng Tan, and Roman Krahne*

The soft hybrid organic–inorganic structure of two-dimensional layered perovskites (2DLPs) enables broadband emission at room temperature from a single material, which makes 2DLPs promising sources for solid-state white lighting, yet with low efficiency. The underlying photophysics involves self-trapping of excitons favored by distortions of the inorganic lattice and coupling to phonons, where the mechanism is still under debate. 2DLPs with different organic moieties and emission ranging from self-trapped exciton (STE)-dominated white light to blue band-edge photoluminescence are investigated. Detailed insights into the directional symmetries of phonon modes are gained using angle-resolved polarized Raman spectroscopy and are correlated to the temperature-dependence of the STE emission. It is demonstrated that weak STE bands at low-temperature are linked to in-plane phonons, and efficient room-temperature STE emission to more complex coupling to several phonon modes with out-of-plane components. Thereby, a unique view is provided into the lattice deformations and recombination dynamics that are key to designing more efficient materials.

1. Introduction

Color tunability of the emission from a single material is an attractive property of two-dimensional lead-halide layered perovskites (2DLPs) towards solid-state lighting applications.[1–9] This feature can emerge from the coincidence of the band edge emission with a broad emission band below the band gap that results from defects or self-trapped excitons (STEs).[7,10–12] The

self-trapping of excitons occurs due to local lattice deformations that are induced by the Coulomb-field of the electron-hole pair itself.[13] Such STE formation is favored in distorted octahedra lattices, and was first observed in 2DLPs with (110)-oriented octahedra lattices, which have intrinsically a strongly corrugated structure.[14,15] With the use of specific organic cations that induce static distortions in the octahedra lattice, STE formation and broadband emission can also be observed from 2DLPs with the more typical (001) crystallographic orientation,[8,11,16] where out-of-plane distortions were identified as a critical structural property.[10] Recent theoretical studies elucidated that Jahn–Teller like lattice deformations lead to the effective formation of STEs, and confirmed that out-of-plane distortions result in more efficient STE emission.[17]

The local lattice deformation related to the STE requires energy, and several works have investigated the energy barrier for STE formation in different layered perovskite systems.[5,7,13,18,19] It is common understanding that phonons are involved in the formation of STEs and their emission dynamics in 2DLPs, however the detailed mechanism is not clear.[20–24] In 3D perovskites, the electron-phonon coupling can be assigned to strong longitudinal-optical (LO) phonons and has been quantified by

---

M.-L. Lin, Y.-C. Leng, P.-H. Tan
State Key Laboratory of Superlattices and Microstructures
Institute of Semiconductors
Chinese Academy of Sciences
Beijing 100083, China
M.-L. Lin, Y.-C. Leng, P.-H. Tan
Center of Materials Science and Optoelectronics Engineering & CAS
Center of Excellence in Topological Quantum Computation
University of Chinese Academy of Sciences
Beijing 100049, China

B. Dhanabalan, G. Biffi, S. Kutkan, R. Krahne
Optoelectronics Research Line
Istituto Italiano di Tecnologia (IIT)
Via Morego 30, Genoa 16163, Italy
E-mail: roman.krahne@iit.it
B. Dhanabalan, M. P. Arciniegas
Nanochemistry
Istituto Italiano di Tecnologia (IIT)
Via Morego 30, Genoa 16163, Italy
E-mail: milena.arciniegas@iit.it
G. Biffi
Materials Physics Center
Spanish National Research Council
Paseo Manuel de Lardizabal 5, Donostia-San Sebastián 20018, Spain

**ADVANCED
SCIENCE NEWS**

www.advancedsciencenews.com

NANO · MICRO

small

www.small-journal.com

the Huang–Rhys factor.[25,26] However, in 2DLPs, in particular with single octahedra layers, the vibrational mode spectrum is highly complex, and the lattice distortions are very different from their 3D counterparts.

Vibrations in 2DLPs can be analyzed in terms of oscillations of molecular bonds (for example Pb–Br stretching or scissoring), or as oscillations of subunits (for example rocking/twisting motions of the $PbBr_6$ octahedra) to which specific symmetry groups can be assigned.[27–29] On the other hand, the resemblance of 2DLPs to solid-state crystals allows to interpret certain vibrational resonances as optical or acoustic phonon modes of a lattice. For example, some out-of-plane vibrations have been associated to LO phonons,[30–33] while the organic/inorganic bilayer structure forms a superlattice that could lead to back-folding of acoustic phonons.[31] Concerning vibrations across the bilayer structure, cross-plane coherent acoustic phonons have been also reported.[34,35] The organic layer determines the distortions of the inorganic layer, and thereby influences the optical and vibrational properties of the 2DLPs.[8,28,29,36] Vibrational bands related to the organic moieties that appear at higher frequencies can also impact the band edge emission process.[33,37]

With regard to the broadband emission of 2DLPs, there is still an ongoing debate if, and to what extent, structural defects and phonons are involved in the recombination process, either directly as emissive centers, or indirectly by assisting in the formation of STEs.[12,24,38] Therefore, a combined experimental study of both the STE emission and the low-frequency modes in 2DLP systems is of great interest.

Here, we investigate a set of Ruddlesden–Popper 2DLPs with single layer inorganic Pb–Br octahedra lattices, but different organic cations (short and long primary and secondary amines) that lead to different lattice deformations and different emission color. The optical properties of our samples comprise broad emission at room temperature, broad emission in distinct low temperature ranges, and solely blue band edge emission for room temperature or below. With polarized and angle-resolved Raman measurements, we are able to distinguish in- and out-of-plane vibrations, resolving uniaxial and biaxial symmetries of the in-plane vibrational components that have been so far neglected in the phonon coupling process of 2DLP broadband emitters. Through temperature-dependent photoluminescence analysis, we observe multiple STE bands in all the samples, which are likely to originate from different electron-phonon coupling mechanisms. The appearance of broad emission bands with weak intensities at temperatures below 100 K points to STE coupling to phonon bands with strong in-plane components, since the thermal range corresponds to the energies of these phonon bands. Interestingly, for the undistorted primary ammonium 2DLPs we observe a single STE band at low temperature, while for the samples prepared with secondary amines clearly two bands can be distinguished. This could be related to their more distorted lattice with respect to primary ammonium samples, indicating an in-plane degeneracy with respect to deformation that is induced by the organic cations. The 2DLPs synthesized with secondary amines also manifest a strong STE band in the range from 200–300 K. The high emission intensity points to out-of-plane Jahn-Teller deformations,[17] and consequently to coupling to out-of-plane phonon modes. For these samples, we observe phonon modes with out-of-plane symmetry at energies around 80–120 cm^{-1} (10–15 meV), however, with much weaker intensity than the modes with in-plane symmetries. The rich vibrational spectra that do not feature a dominant optical phonon mode point to complex electron-phonon coupling mechanisms for efficient STE emission, and the tilted configuration of the $PbBr_6$ octahedra in the 2DLP lattice most likely enables coupling to the out-of-plane vibrational components of a variety of modes.

2. Results and Discussion

2.1. Structural Symmetries in 2DLPs Synthesized with Primary and Secondary Amines

For our study, we selected a set of four different (single octahedra layer) Ruddlesden Popper 2DLPs, two of which were synthesized with primary, and two with secondary amines as organic cations. Furthermore, in both systems we varied the length of the aliphatic chain. We note that with the primary ammoniums we obtained stable layered perovskites already by using molecules with short aliphatic chains (butylammonium (BA) with 4 carbon segments (4C)), while for secondary ammoniums longer aliphatic chains of at least 10C were needed to form a stable layered structure, as reported in our previous work.[8] Thus, we discuss single layer lead-bromide 2DLPs with BA (4C) and UDA (undecylammonium, 11C) as primary ammoniums, and with N-MDA (N-methyldecylammonium, 10C) and N-MDDA (*N*-methyldodecylammonium, 12C) as secondary ammoniums. **Figure 1** shows the crystallographic structure and photoluminescence (PL) spectra of $(BA)_2PbBr_4$, $(UDA)_2PbBr_4$, $(DA)_2PbBr_4$, and $(N-MDDA)_2PbBr_4$ (see Section S1 in the Supporting Information for details). These very different organic cations lead to different distortions of the octahedral lattice (as can be seen in the side and top view projections in Figure 1b). In particular, for the primary ammoniums the octahedra are strongly misaligned in the octahedra plane, and in the case of BA their lattice shows no out-of-plane distortion. Structures synthesized with longer primary ammoniums (DA/UDA) feature similar in-plane misalignment of the octahedra, but also a small out of plane distortion. In contrast, the structure of the secondary ammonium sample with N-MDDA shows good in-plane alignment of the octahedra, and a much stronger out-of-plane distortion. The different lattice distortions result in very different emission properties, as is evident in Figure 1c. The PL of the BA sample is dominated by band edge emission, and no broad emission band at longer wavelength is observed, while the PL spectra of the UDA and N-MDDA samples (which feature octahedra tilting, see side views in Figure 1b) show a pronounced broad emission band that spans across the full visible spectral range. The broadband STE emission in our materials originates from a transient distortion of the octahedra lattice that can be seen as an excited state defect. It can be interesting to consider if and how the static distortions induced by the organic ligands could favor the generation of such excited defect states. Density-functional-theory (DFT) modeling (performed for $T = 0$ K)[8] shows that the organic moieties connect to the octahedra lattice by hydrogen (H)-bonds. The number and the connectivity of such H-bonds depend on the type of organic ligand. Different ligands should favor such excited-state defects only if they cause related distortions within the octahedral lattice. We find that for primary amines the formed
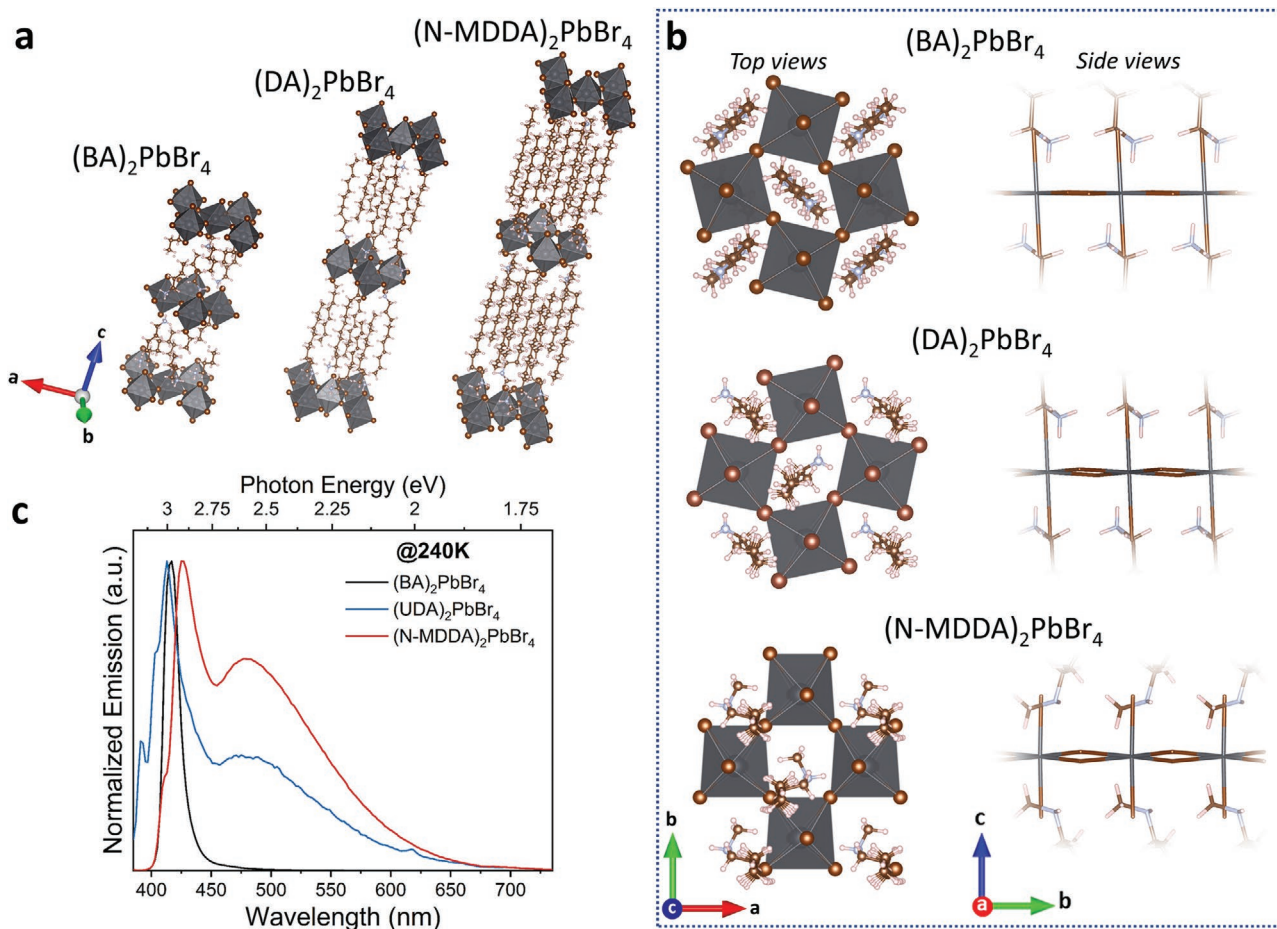
Figure 1. Two-dimensional layered perovskites with different organic cations. a) Visualization of the structure of Ruddlesden–Popper 2DLPs with different types of organic cations using VESTA software:[40] BA and DA as primary ammoniums,[27,41] and N-MDDA as secondary ammonium.[8] b) Top and side views on the $(BA)_2PbBr_4$, $(DA)_2PbBr_4$ and $(N\text{-}MDDA)_2PbBr_4$ structures evidencing the differences in in-plane octahedra alignment and out-of-plane distortions. The structure of the $(DA)_2PbBr_4$ is used to infer lattice distortions of the inorganic layer in UDA samples. Figure S5 (Supporting Information) reports in-plane angles for these materials. c) PL spectra recorded from 2DLP powders at 240 K that evidence the impact of the organic cations on the emission properties.

H-bonds result in in-plane distortions, as they create strong deviations from the 180° in-plane angle. For the secondary amines the organic moieties lead to a compression of the octahedra void and to significant tilting of the octahedra (as shown in Figure 1). This static deformation is mainly concentrated off the octahedra lattice plane, and therefore should favor excited-state defects in the out-of-plane direction.

Microscopy images, X-ray diffraction and absorbance spectra are shown in Figures S1 and S2 (Supporting Information), and PL spectra including the N-MDA sample at 240 and 60 K are reported in Figure S3 (Supporting Information). We note that for all samples the blue band edge emission consists of multiple peaks in agreement with our previous work.[39]

2.2. Polarized and Angle-Resolved Ultralow-Frequency Raman Spectroscopy

To get insights into how the crystallographic structures discussed above might influence the phonon modes of the

different 2DLPs, we have performed micro-Raman spectroscopy on single platelets that were deposited on Si/SiO_2 substrates by mechanical exfoliation or direct deposition of the platelets from powders. In our previous study, we demonstrated that the thickness of the platelets does not influence the frequency of the Raman peaks.[29] Figure S6 (Supporting Information) outlines the experimental setup for the angle-resolved and polarized Raman spectroscopy that includes both linear polarizer and analyzer in excitation and detection, respectively, and a rotational $\lambda/2$ wave plate in the combined beam path. **Figure 2**a illustrates the two different polarization configurations in this experiment with respect to the orientation of single flakes of crystalline materials. Parallel (VV) and orthogonal (HV) orientation of the polarizer and analyzer enables to measure the polarized (VV) and depolarized (HV) Raman signals. The rotational $\lambda/2$ wave plate allows to vary the orientation of the polarized beams with respect to the in-plane axes of the sample. It can be shown that the rotation of the wave plate by an angle $\theta/2$ is equivalent to a rotation of the sample by θ
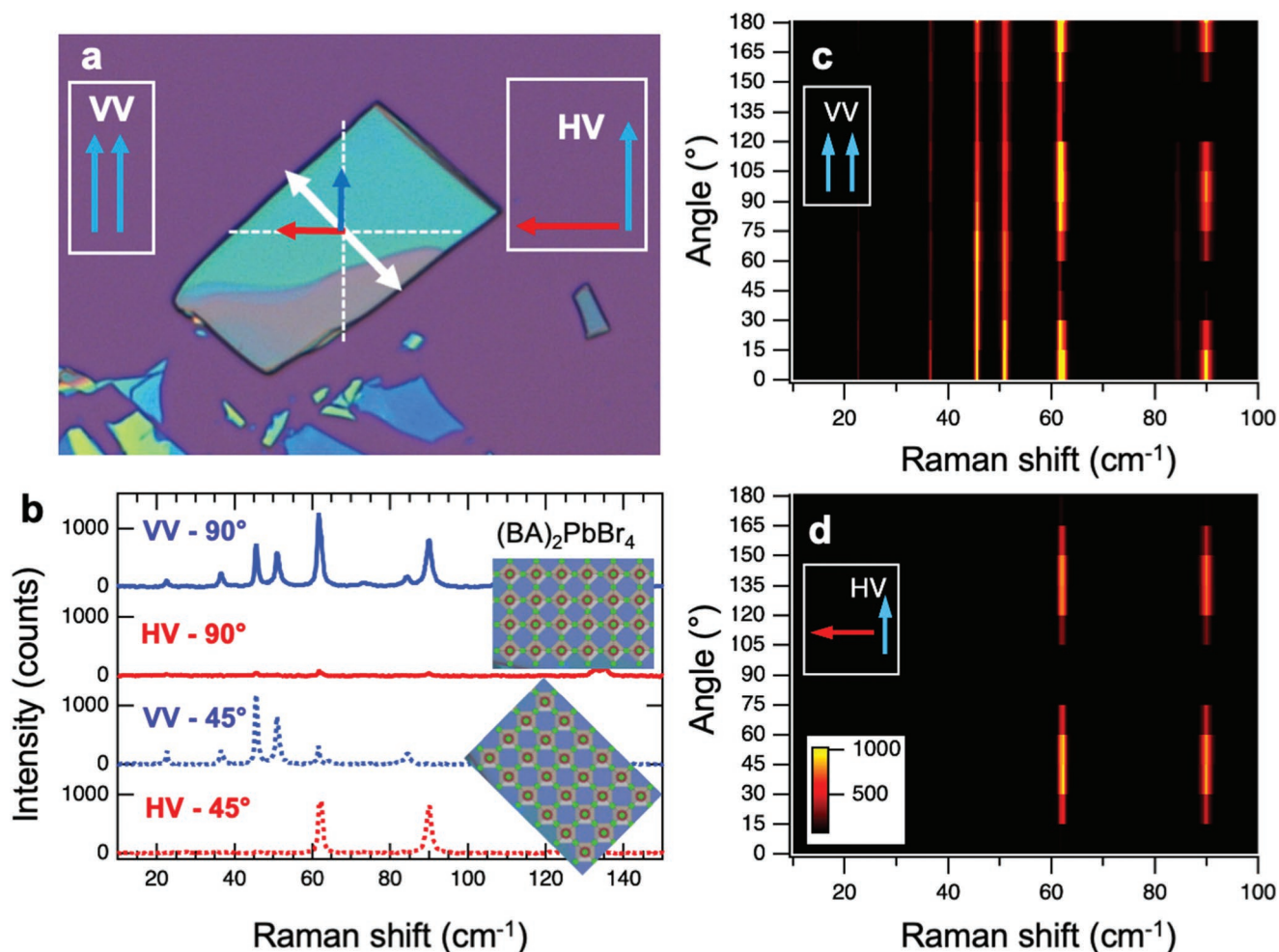
Figure 2. Angle-resolved polarized micro-Raman spectroscopy on single 2DLPs. a) Optical microscope image of an exfoliated $(BA)_2PbBr_4$ flake together with illustrations of the polarized (VV) and depolarized (HV) components of a unidirectional vibration along a principal lattice axis under linearly polarized excitation. b) Raman spectra recorded at a temperature of 5 K under (VV) and (HV) configurations from a $(BA)_2PbBr_4$ flake at two different orientations, as depicted in the insets. c,d) Color maps of the Raman intensity recorded at 5 K of $(BA)_2PbBr_4$ versus Raman shift and rotational angle for c) VV (polarized) and d) HV (depolarized) configurations. The angle is taken with respect to the direction of the vertical (V) polarizer. Clearly, different sets of peaks show different angular intensity dependence: i) some modes appear only in VV and are absent in HV, ii) some modes appear with one, other with two angular dependent maxima, iii) for some modes, the maxima of the peaks appear 45° shifted in HV with respect to VV. Color legend in (d) is valid for (c,d).

with respect to the orientation of the linear polarizer and analyzer.[42] This approach has the advantage that it maintains the same probing spot and therefore allows for a straightforward analysis of the angular intensity behavior of the vibrational modes. In the following, we consider θ as the rotational angle of the sample for simplicity of the discussion. As an example of the directional information that we can extract, we show in Figure 2a a 2DLP flake that is oriented at roughly 45° to the V and H directions. The white arrow illustrates a vibration parallel to the short edge orientation of the flake, and the blue and red arrows give the VV and HV components of this mode. We can easily imagine that if the sample is rotated clockwise by 45°, then this mode will appear only in VV and not in HV (Figure 2b). This behavior gives rise to the angle-dependent Raman intensity of the modes that we observe, which is plotted for a $(BA)_2PbBr_4$ flake in Figure 2c,d. Clearly, a larger number of modes appear in polarized (VV) configuration,

and for the modes that are present in both polarization configurations, for example at 61 cm⁻¹ and 84 cm⁻¹, their intensity maxima are shifted by 45° between VV and HV experiments (see Figure S7 in the Supporting Information). Figure S8 (Supporting Information) shows the angle-dependent color plots of the Raman spectra for the other samples discussed in this work.

2.3. Symmetries and Origins of Vibrational Bands in 2DLPs

We investigated the vibrational response in the ultralow-frequency range from 10 to 140 cm⁻¹, where the majority of the inorganic lattice resonances can be found. We focus on the low-temperature characterization, since at 5 K the peaks in the Raman spectra are more clearly resolved than at room temperature. Raman spectra recorded at higher temperatures
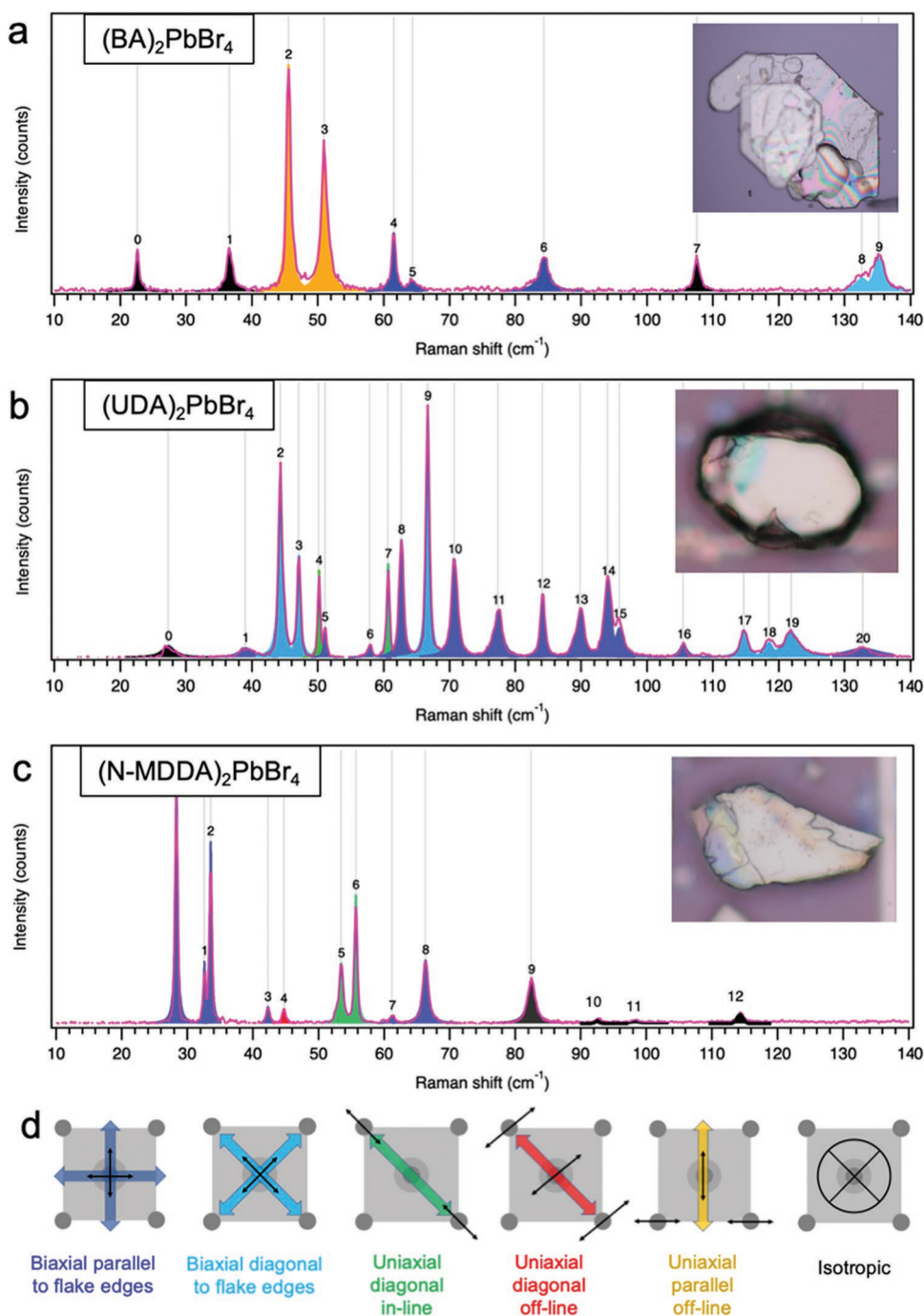
Figure 3. Raman spectra of 2DLPs synthesized with different organic cations, and color coding of the vibrational symmetries. a–c) Raman spectra recorded from single 2DLP flakes at 5 K. The observed peaks are color coded as described in the main text and Table 1. Images of the investigated flakes are shown in the insets. d) Illustration of the color coding and directionality of the modes. A top view on a single PbBr$_6$ octahedron is sketched in grey colors. Broad colored arrows give the directions of maximum intensity of the modes in VV configuration, and black arrows indicate a plausible motion of the metal–halide atoms.

are reported in Figures S9 and S10 (Supporting Information), where a broadening and a slight red-shifting of the phonon modes is observed with increasing temperature. **Figure 3**a–c shows the Raman spectra recorded at 5 K for the primary and secondary ammonium samples introduced in Figure 1, together with a Lorentzian fitting of the peaks. We note that

experiments on different platelets from the same batch give very similar spectra, with variations in peak position below 1 cm^{-1}, and that all peaks are sharp and have well-defined Lorentzian shapes as expected from single crystalline structures. The color filling of the peaks with blue, green, red, orange and black marks their different directional behavior

Table 1. Color coding to label the mode symmetries, and angle-dependent maxima with respect to the rotational orientation of the platelets (i.e., angular orientation to the vertical polarizer). Offsets caused by small misalignment of the flakes from the orthogonal axes (V/H) were subtracted for clarity. The presence (✓) or absence (✗) of each mode is indicated for all samples.

Color code	Mode symmetry		Max. Intensity at angle		Present in			
			VV	HV	$(BA)_2PbBr_4$	$(UDA)_2PbBr_4$	$(N-MDA)_2PbBr_4$	$(N-MDDA)_2PbBr_4$
▉	In-plane	Biaxial	0°, 90°	45°, 135°	✓	✓	✓	✓
▉	In plane	Biaxial	45°, 135°	90°, 180°	✓	✓	✗	✗
▉	In-plane	Uniaxial	135°	90°, 180°	✗	✓	✓	✓
▉	In-plane	Uniaxial	135°	45°, 135°	✗	✗	✓	✓
▉	In-plane	Uniaxial	0°	0°, 90°	✓	✗	✗	✗
▉	Out-of-plane	Isotropic	✗	✗	✓ (low+ high freq.)	✓ (low freq.)	✓ (high freq.)	✓ (high freq.)

that we extracted from the peak intensity with respect to the rotational angle of the sample from 0° to 180° (see **Table 1** for details).

Figure 3d illustrates the direction of maximum intensity in VV by the broad colored arrows, and the black arrows indicate possible motions of the Pb^{2+} and Br^- ions. Dark blue corresponds to two maxima at angles that are parallel/orthogonal to the straight edges of the flake, bright blue to two maxima in the diagonal direction. This points to modes with a biaxial symmetry with respect to the octahedra lattice. For both, the maxima in HV occur at 45° difference in angle with respect to VV, corresponding to a linear oscillatory motion (see Figure S7 in the Supporting Information). Modes marked in green, red and orange feature only one angular maximum, thus unidirectional symmetry. The green mode has the maximum in VV at 45°, and also shows the maxima in HV shifted by 45° with respect to VV, therefore we assigned a linear oscillation in diagonal direction. The red mode has the maximum in VV also in the diagonal direction, however, the maxima in HV occur at the same and orthogonal angles. Therefore, this oscillatory motion must include components at orthogonal angles, which is the case for the illustrated Br-Pb–Br bond bending in the red scheme in Figure 3d. The orange modes show a similar angular behavior, but the directions are rotated by 45°, which indicates Br–Pb–Br scissoring as the probable origin. Finally, the black modes have nearly constant intensity versus angle in VV, and are absent in HV, which corresponds to a classic isotropic behavior, and is in agreement with an out-of-plane oscillation.

With this understanding of the symmetries, we now interpret the phonon bands of the different 2DLPs in detail. The lowest frequency modes in the primary ammonium 2DLPs have isotropic symmetry (Figure 3a,b), which is in agreement with an extension/contraction (breathing) mode of the $PbBr_6$ octahedra that show negligible or small out-of-plane tilting (see side views in Figure 1b).[28,29] For UDA we observe a single peak (at 27.3 cm^{-1}) with this symmetry, while for the much shorter BA two peaks appear (at 22.6 and 36.5 cm^{-1}). This points to a splitting of this octahedra vibration mode through inter-layer

coupling that is mediated by the organic spacers. And indeed, we observe coupled vibrational motions of the $PbBr_6$ octahedra in our DFT simulations, as evidenced in the Movies M1–M3 in the Supporting Information. For the 2DLPs with secondary ammonium cations the behavior is different, and the lowest frequency modes show a clear biaxial symmetry (dark blue). This symmetry along the directions of the straight edges of the exfoliated flakes can be understood by a rocking motion of the $PbBr_6$ octahedra, which are well aligned in-plane and tilted out-of-plane (top view in Figure 1b). The triplet of peaks in the range from 25 to 35 cm^{-1} points to a lifted degeneracy of the octahedra vibrational modes that could stem from their tilting and static distortion.

The lowest frequency modes in a superlattice architecture can also result from backfolding of acoustic phonons in out-of-plane direction. Such analysis has been reported for 2DLPs with iodide as halide anion, and the series of backfolded mode frequencies has been analyzed in the frame of the Rytov model,[31,43] in which the zone-folded acoustic mode dispersion can be approximated by a continuum model

$$\cos(kd) = \cos\left(\frac{\omega d_1}{v_1}\right)\cos\left(\frac{\omega d_2}{v_2}\right) - \frac{1+\kappa^2}{2\kappa}\sin\left(\frac{\omega d_1}{v_1}\right)\sin\left(\frac{\omega d_2}{v_2}\right), \; \kappa = \frac{\rho_1 v_1}{\rho_2 v_2}$$

(1)

where $d_{1,2}$, $v_{1,2}$, and $\rho_{1,2}$ are the thicknesses, sound velocities, and densities of the inorganic (1) and organic (2) layers. We tested this model for the Raman bands that we observe, but by using bulk elastic parameters for the organic and inorganic layers we did not obtain reasonable agreement with our data.

We then hypothesized that the elastic modulus of the organic layers in the 2DLPs could be different from that extracted from the ligand coated nanocrystals reported in literature.[44] In particular, the interactions between long organic molecules in the van der Waals gap could lead to strongly increased stiffness, and therefore to increased sound velocity.[45] Note that here we consider the stiffness of the organic layer separately, and that longer molecules give rise to a larger number of lateral van der

Table 2. Peak frequencies obtained by Lorentzian fitting as shown in Figure 3 for the different 2DLPs. The frequencies obtained by the Rytov model using Equation (1) are reported for each material. Resonant modes with biaxial symmetry appear also at higher frequencies, and for certain sets (for example blue peaks in (N-MDA)$_2$PbBr$_4$ at 29, 33, 35 cm^{-1}) higher modes with similar symmetry are found at approximately twice the frequency of the lower mode, indicating the presence of higher order modes.

2DLP type			Peak frequency [cm^{-1}]
Primary amines	4C	(BA)$_2$PbBr$_4$	23 37 46 51 62 64 73 84 108 133 135
		Rytov freq., v_2=960	22 40 62
	10C	(UDA)$_2$PbBr$_4$	27 39 44 47 50 51 58 60 63 67 71 77 84 90 94 96 105 115 119 122 133
		Rytov freq., v_2=2700	27 42 68
Secondary amines	10 C	(N-MDA)$_2$PbBr$_4$	29 33 35 45 47 53 57 60 65 70 78 82 116
		Rytov freq., v_2=2340	29 46 73
	12C	(N-MDDA)$_2$PbBr$_4$	28 33 34 42 45 53 54 56 61 66 82 93 98 115
		Rytov freq., v_2=2530	28 45 72

Waals interactions in the gap, leading to increased stiffness.[44] By taking the sound velocity in the organic layer (v_2) as adjustable parameter, we achieved relatively good agreement with the lowest frequency peaks, as reported in **Table 2**. Note that we consider the first backfolded mode, while Dahod et al.[31] interpreted the lowest frequency modes in their experiments as the fourth backfolded branch (using bulk parameters). Although we obtained good agreement of the first backfolded branch with the lowest frequency peaks for our samples by applying a reasonable adjustment of v_2, we have reservations regarding this interpretation of the lowest acoustic modes in 2DLPs. The reason is that this model has so far only been applied to low-dimensional perovskites with a larger number of connected octahedra layers,[31] where the thickness of the inorganic layer is better defined. Also, for single layer systems with a lattice of symmetric and nontilted octahedra, the Rytov model might be seen as a different description of cross-plane coupling of the vibrational modes of the octahedra. However, tilted and distorted octahedra networks are already too complex to be described by this simplistic model that assumes homogeneous layers. And indeed, for secondary ammonium 2DLPs, we observe sets of Raman peaks in this low-frequency regime with distinct in-plane symmetries, which cannot be accounted for by the Rytov model, but are reasonable when interpreted as degenerate rocking modes as discussed in the previous paragraph.

Continuing our analysis with the Raman peaks at higher frequencies, we observe bands with red (N-MDDA, 44.7 cm^{-1})) and orange (BA, 45.5 cm^{-1}, 51.0 cm^{-1}) symmetry behavior that we attribute to Pb–Br bond bending and scissoring in agreement with literature.[24,28,29] Concerning (UDA)$_2$PbBr$_4$, the large number of peaks, mostly with biaxial symmetry, is surprising, which goes along with the absence of peaks that have maxima in VV and HV at same angles. A plausible explanation could be that the slight tilting of the octahedra leads to modes with biaxial symmetry, while the nearly undistorted octahedra bond angles could favor the generation of a large set of modes, similar to bulk perovskite crystals.[46,47] At frequencies around 50–60 cm^{-1} we observe the (green) uniaxial mode in the both primary and secondary ammonium 2DLPs with long aliphatic chains. Both the frequency range and the symmetry behavior agree with Pb–Br stretching as their origin.[24,28,29] Different frequencies from Pb–Br bond stretching can also result from

the different oscillatory components: the axial motion of the heavy Pb ion will lead to a mode at lower frequency, and that of the lighter Br ion to a higher frequency mode, a behavior that we also observe in our density-functional theory modeling.[29] Finally, we observe vibrational modes marked in black that are absent in depolarized (HV) spectra, and which therefore show the signature of isotropic modes. Both the appearance at high frequency (around 80–120 cm^{-1}) and the isotropy with respect to the rotation of the octahedra plane point to out-of-plane vibrations, like Pb–Br bond stretching in the cross-plane, and resemble the vibrational modes with A$_g$ symmetry that were assigned to LO phonon modes. Interestingly, such behavior (absence in HV) is not observed for the high frequency modes in (UDA)$_2$PbBr$_4$.

Since the octahedra lattices of the 2DLPs have biaxial symmetry (as depicted in Figure 1), the appearance of the red, orange and green modes with uniaxial symmetry is somewhat puzzling. One possible explanation is an asymmetry that is introduced by the organic layer, thus by the accommodation of the head group of the organic cation in the octahedra void, or tilting angles of their aliphatic chain. This could result in enhanced coupling to the Pb–Br vibrational modes in one octahedra lattice direction with respect to the other. The two samples with secondary ammoniums show similar vibrational mode spectra (see Figures S8 and S11 in the Supporting Information), as would be expected for the relatively small difference in aliphatic chain length of 2C. Nonetheless, there are distinct differences, in particular, regarding the lowest frequency band (that should be related to the octahedra rocking/twisting), and in the band around 84 cm^{-1} that shows isotropic character and should be related to out-of-plane oscillations. For the latter, we find a double-peak feature for (N-MDA)$_2$PbBr$_4$ that could point to mode splitting caused by interlayer coupling, while a single peak is observed for (N-MDDA)$_2$PbBr$_4$.

### 2.4. Phonon Properties and STE Emission

The mechanism of STE formation and emission includes the local deformation of the lattice in vicinity of the electron-hole pair that is induced by the Coulomb field. This distortion shifts the minimum of the energy band with respect to the nuclear

**ADVANCED
SCIENCE NEWS**

www.advancedsciencenews.com

NANO · MICRO

small

www.small-journal.com

coordinate, and enables exciton recombination at much lower energy than the band gap due to the higher potential energy of the ground state in the deformed lattice.[22,25] In this process, energy is needed for the creation of the STE that could stem from the hot exciton itself or from lattice vibrations.[10] Then, with the (sequential) exciton recombination of the STE,[22] the potential energy of the dynamically deformed lattice needs to be dissipated by phonons. An atomistic study revealed that Jahn–Teller (out-of-plane) distortions of the octahedra favor the emission from STEs,[17] and a recent theory work reported that STEs arise from an optical deformation potential that modulates the thickness of the inorganic layer and thereby the confinement potential of the excitons.[24] Apart from the organic layer thickness, also the type of organic moieties determines the dielectric confinement and thereby the exciton binding energy.[48] This in turn could affect the STE formation, as more strongly bound excitons feature a stronger Coulomb field that could interact with the crystal lattice. STE emission, the induced deformation potential and coupling to phonons has been studied experimentally and theoretically in 3D double perovskites,[18,25,26] where a dominant LO phonon mode is observed at around 20–25 meV, and a good correlation of the full-width-half-maximum (FWHM) of the broad emission to the energy of the out-of-plane LO phonons has been reported. This allowed to evaluate the electron–phonon coupling with the Huang–Rhys factor by the relation[18,25,26]

$$FWHM[eV] = 2.36 \sqrt{S} \, \hbar\omega_{phonon} \sqrt{\coth\left(\frac{\hbar\omega_{phonon}}{2k_{\mathrm{B}}T}\right)} \qquad (2)$$

Here S is the Huang Rhys factor, k_{B} is the Boltzmann constant, T is the temperature in Kelvin, and $\hbar\omega_{phonon}$ is the energy of the phonon mode. We note that Equation (2) was derived for electron–phonon coupling related to emission from defects acting as color centers,[49] and indeed, the below bandgap emission in double perovskites is typically attributed to color centers.[32] To test this approach for our set of metal–halide Ruddlesden–Popper perovskites with primary and secondary ammoniums we have investigated their temperature-dependent photoluminescence. **Figure 4**a,d shows color maps of the emission (UDA)$_2$PbBr$_4$ and (N-MDDA)$_2$PbBr$_4$ (spectra of (BA)$_2$PbBr$_4$ and (N-MDA)$_2$PbBr$_4$ are displayed in Figures S12 and S13, Supporting Information respectively), which reveal that the (primary ammonium) UDA sample manifests broad emission around 10–80 K, while the secondary ammonium samples show different broad emission bands below the band gap in different temperature ranges and with significantly different intensities: two weak bands centered around 2.25 and 2 eV are present in the cryogenic range up to 120 K, and a strong broad emission above 200 K is centered at 2.5 eV, which for (N-MDDA)$_2$PbBr$_4$ becomes equal in amplitude to the band edge emission at around 220–240 K. The UDA sample manifests
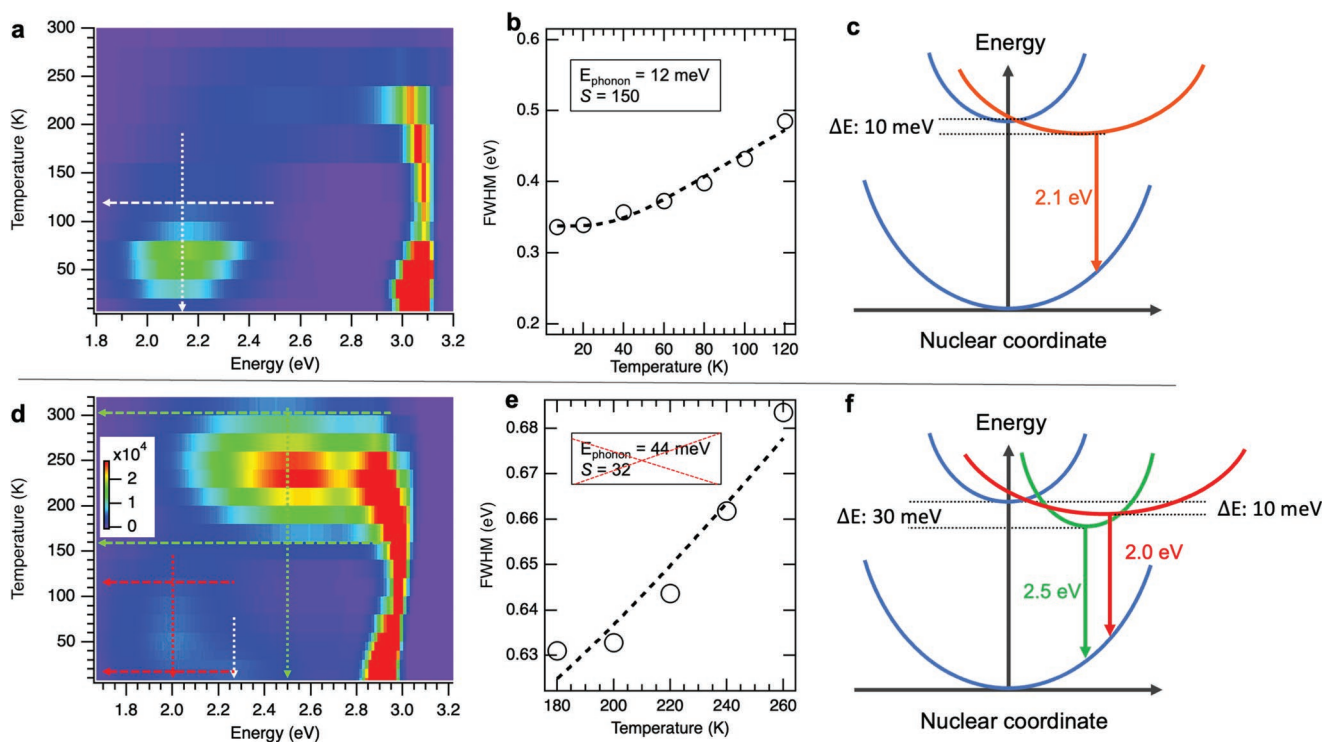

Figure 4. Temperature dependent emission properties of 2DLPs that manifest STE in distinct temperature ranges. a–c) (UDA)$_2$PbBr$_4$, d,e) (N-MDDA)$_2$PbBr$_4$. a,d) Color map of the emission intensity versus energy and temperature. The horizontal arrows indicate the limits of the temperature range of broad band appearance, and the vertical ones mark the central energies of the STE bands. The color legend for the PL intensity in (d) is also valid for (a). b,e) The fitting of the FWHM of the broad emission centered at around b) 2.1 eV and e) 2.5 eV with Equation (2). The legend that is crossed out in red illustrates that in this case the fitting does not work. c,f) Schematic energy structure with trapping/detrapping and emission energies extracted from the temperature dependent emission in (a,d).

**ADVANCED
SCIENCE NEWS**
www.advancedsciencenews.com

NANO · MICRO
small
www.small-journal.com

a single broad emission band with increasing FWHM for increasing temperature, which encouraged us to test the evaluation of the Huang–Rhys factor along Equation (2) (Figure 4b). We obtain a fitting with reasonable accuracy yielding a phonon energy of around 12 meV (96 cm^{-1}) and a Huang–Rhys factor of $S = 150$. However, in view of the rich phonon spectrum that we measured from the (UDA)$_2$PbBr$_4$ flakes, this phonon energy seems to have little meaning since we cannot assign it to a particular mode.

For the broad emission of (N-MDDA)$_2$PbBr$_4$ it is not clear that the fitting of the FWHM versus temperature with Equation (2) can work, since multiple broad emission bands are present (see Figure 4d and Figure S14, Supporting Information). Indeed, for the low temperature STE band no reasonable fitting was possible. We therefore tried the strong STE emission band in the high temperature range (180–280 K). However, as evident in Figure 4e, no accurate fitting could be achieved, and furthermore, no phonon bands are observed for (N-MDDA)$_2$PbB$_4$ at frequencies around 44 meV (350 cm^{-1}) that would correspond to the fitting result. In fact, no phonon modes are detected in the range from 160 to 500 cm^{-1} (Figure S15, Supporting Information). We therefore conclude that for the secondary ammonium with strong STE emission the conditions to quantify electron–phonon coupling with Equation (2) are not fulfilled. One reason could be that the spectrum in Figure 3c does not manifest a dominant LO phonon mode as it is the case for bulk crystals.[18,25,26] In 2DLPs the out-of-plane motion of LO-phonons could be dampened by the organic layers in the inorganic/organic layered architecture. Since nevertheless strong STE emission occurs in 2DLPs like (N-MDDA)$_2$PbBr$_4$, we conclude that more complex electron–phonon coupling mechanisms must be at work that could involve multiple phonon modes. For example, in addition to the LO phonons marked in black in Figure 3c, the unidirectional modes observed with high intensity in (N-MDDA)$_2$PbBr$_4$ (marked in green) could play a role. Their oscillation could stem from stretching of the tilted vertical Pb–Br bonds and thereby be relevant for efficient STE emission, that is, favoring out-of-plane Jahn–Teller distortions.[17]

From the broad band emission shown in Figure 4a,d and Figure S13 (Supporting Information) we can extract upper and lower boundaries of the temperature ranges in which the STE bands appear. Furthermore, the STE trapping/detrapping barriers can be determined from the temperature dependence of the intensity ratio between the band-edge exciton and STE emission.[5,11,22,50] We sketch the energy dispersion for the band edge and STE emission versus the dynamic deformation (i.e., the nuclear coordinate) in Figure 4c,f and assign the lower bound of the observed emission band to the height of the trapping barrier (band edge (central) minimum to intersection with the STE dispersion), and the upper bound to the detrapping barrier (minimum of STE dispersion to intersection with band edge dispersion). From the central wavelength of STE emission we can also extract some qualitative information on the relative curvature of the STE dispersion, since the energy differences from excited to ground state in the schemes in Figure 4c,f need to be consistent. For (UDA)$_2$PbBr$_4$ in Figure 4c we obtain a detrapping barrier of 10 meV (80 cm^{-1}) that agrees fairly well with the phonon energy of 12 meV derived by Equation (2). For (N-MDDA)$_2$PbBr$_4$ we observe multiple broad emission bands
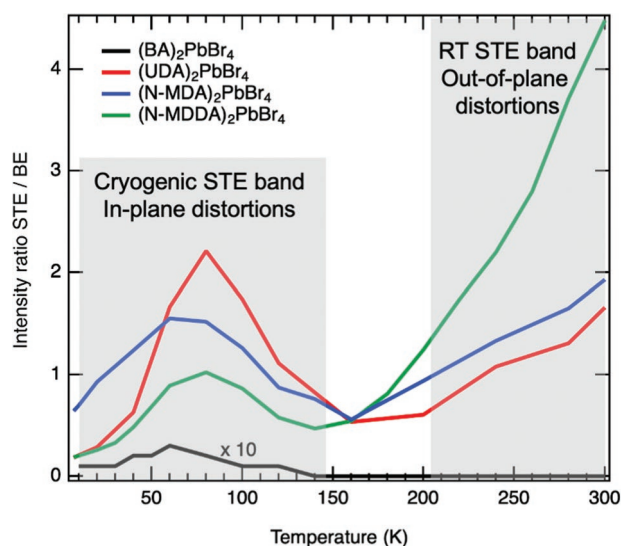
Figure 5. Low- and high temperature STE emission. Intensity ratio of the STE emission bands with respect to the band edge (BE) emission. For all samples a local maximum around 50–80 K is found that we associate to STE emission from in-plane distortion of the octahedra.

in different temperature ranges: two weak ones at cryogenic temperatures (20–120 K), and a strong one at 160–300 K, that also appear at different emission wavelengths (see Figure 4d). Extracting the energy barriers for detrapping that reflect the depth of the STE dispersion minimum, we obtain 10 meV for the weak low-temperature band centered at 2 eV and 30 meV for the strong high-temperature band (see Figure S16 in the Supporting Information).

The intensity ratio between the STE and the band edge emission plotted in **Figure 5** confirms the existence of different low- and high temperature bands. Here we find for all samples a local maximum at a temperature around 80 K, thus distinct STE emission occurs in a temperature range from 40 to 100 K, corresponding to an energy range of 3–8 meV (25–70 cm^{-1}). These energies match the frequency region in which the dominant in-plane phonons occur (see Figure 3b,c), and therefore in-plane Jahn-Teller distortions that lead to electrons and holes trapped in neighboring octahedra[17] are a highly probably mechanism underlying this STE emission with low efficiency. At temperatures above 150 K, the STE contribution increases again (Figure 5), and this threshold between low- and high temperature STE emission corresponds to a thermal energy of 12 meV, thus around 100 cm^{-1}. This coincides with the range where the out-of-plane phonons were observed (80–130 cm^{-1}) in Figure 3 (see also Table 2), and therefore we conclude that for higher temperatures the STE emission process is facilitated by out-of-plane distortions that are known to lead to more efficient STE emission. For the secondary ammonium samples, in particular (N-MDDA)$_2$PbBr$_4$, the high temperature STE outperforms the low-temperature one. The black color coded out-of-plane LO phonon modes are observed in the range from 80 to 120 cm^{-1}, therefore also this correlation of the optical and Raman data supports the coupling of the high-energy STE emission to these out-of-plane phonon bands. Time-resolved PL experiments show similar decay traces for the band edge emission and STE

**ADVANCED
SCIENCE NEWS**

www.advancedsciencenews.com

**NANO · MICRO
small**

www.small-journal.com

at room temperature,[8] while at low temperature the STE bands manifest a much slower decay up to the microsecond range (Figure S17, Supporting Information), in agreement with ref. [5].

3. Conclusion

We mapped the different symmetries of the vibrations in 2D lead bromide layered perovskites that show different color emission with angle-resolved polarized Raman spectroscopy and found that their low-frequency phonon spectrum is dominated by modes with strong in-plane symmetry. We identified modes with biaxial, uniaxial and isotropic directionality with respect to the octahedra lattice that are strongly connected to the static lattice deformations induced by the organic cations. In 2DLPs synthesized with secondary amines that feature significant octahedra tilting, the low-frequency octahedra rocking modes show biaxial symmetry, while for the primary ammonium samples they are isotropic. The uniaxial directionality of some Pb–Br bending and stretching modes is likely to be induced by the asymmetric conformation of the A-cations in the organic layer, since the symmetry of the inorganic lattice is biaxial. We find that the highly anisotropic architecture of 2DLPs translates to a very different phonon spectrum with respect to their bulk counterparts, with strongly reduced intensity of the out-of-plane LO phonon mode, and more in-plane modes at low-frequencies. These different elastic properties affect the electron-phonon coupling and the process of STE formation and relaxation, and therefore their emission color. While 2DLPs with primary ammoniums show a single STE emission band that has maximum intensity at cryogenic temperatures and is weak at room temperature, the secondary ammonium samples feature multiple STE emission bands that originate from coupling to in-plane and out-of-plane vibrational modes. Accordingly, we do not observe a clear relation of one LO phonon mode to the STE emission as it was reported for bulk perovskite systems. However, the STE intensity and temperature range in which it appears points to coupling to out-of-plane phonon modes that favor vertical lattice distortions, while the weak STE bands at low temperature should stem from in-plane phonons and distortions that we tentatively associate to electron-hole trapping in neighboring octahedra. This interpretation is corroborated by a good matching of the respective phonon energies with the trapping/detrapping barriers that we extracted from the temperature dependent emission spectra. Our combined study of the vibrational and optical properties of 2DLPs at different temperatures therefore provides deep insights into the dynamics of the white emission of such materials, which is crucial to improve their emission efficiency and for device engineering.

4. Experimental Section

Synthesis: The samples were prepared by following the previous synthesis protocol[8,39] and using two representative organic cations from the primary and secondary amine families, with a short and a long carbon chain: *N*-butylamine, *N*-undecylamine, *N*-methyldecylamine, and *N*-methyldodecylamine. Briefly, 60 μL of HBr were added to 95.5 mg of PbBr$_2$ in a vial, followed by the addition of 1 mL of acetone. The mixture was strongly shaken forming a transparent solution. Next, an aliquot

equivalent to 0.62 mmol of the selected amine was injected into the mixture and the crystals were formed within few minutes. The crystals were collected by centrifugation after 30 min under strong magnetic stirring and washed three times with acetone and dried overnight on filter paper.

Mechanical Exfoliation: The crystals were exfoliated by first placing them on a silicone-free blue adhesive plastic tape (1007R from Semiconductor Production Systems). Gently, a clean part of the tape was pushed onto the platelet deposit. The tape was then detached collecting thin crystals that were transferred to Si/SiO$_2$ substrates for the experiments.

Photoluminescence: PL measurements were performed with an Edinburgh Instruments (FLS920) fluorescence spectrometer equipped with laser diodes and a Xenon lamp coupled to a monochromator for steady-state PL excitation. Room temperature PL spectra were collected with an excitation wavelength of 375 nm with 1 nm spectral resolution and 0.5 s dwell time. Temperature dependent PL measurements were done in an optical cryostat from ARS using optical fibers and excitation with a pulsed laser diode at 375 nm.

Raman Spectroscopy: Raman experiments were performed in an optical cryostat under nonresonant conditions with 632.8 nm excitation wavelength from a He–Ne laser. The spectra were collected in a backscattering geometry using a home-modified Jobin–Yvon HR800 Raman system equipped with an electron multiplying charged-coupled detector (CCD) and a 50 × objective (numerical aperture of 0.45) with long working distance. A 2400 lines mm^{-1} grating was used yielding a spectral resolution of 0.19 cm^{-1} per CCD pixel under 632.8 nm excitation. The laser plasma lines were removed by Bragg-volume-grating-based bandpass filters (BPF) from OptiGrate Corp. A Spectral range down to 5 cm^{-1} was achieved by three BragGrate notch filters (BNF) from OptiGrate Corp with optical density of 3–4 with full width of half maximum of 5–10 cm^{-1}. The angle-resolved polarized Raman spectroscopy measurements were performed in polarized (VV) and depolarized (HV) configurations, where a linear polarizer and analyzer were placed in the incident and scattering paths of the Raman instrument, respectively, along with a λ/2 plate after the polarizer to vary the polarization of incident laser from vertical to horizontal. A second λ/2 plate was allocated in the common path of the incident and scattered light to simultaneously vary the angle of polarization with respect to the sample. Here by rotating the fast axis of the half-wave plate with an angle of *θ/2*, the polarization of incident and/or scattered light is rotated by *θ*. The laser power was kept below 500 μW to avoid laser induced damage. In the temperature dependent measurements, the sample was first cooled to 4 K and then the temperature was raised stepwise to the indicated values.

DFT Modeling: DFT simulations were carried out using the CP2K software.[51] The crystalline structures obtained from XRD analysis were relaxed to the ground-state geometry under tight conditions (10^{-6} Hartree/Bohr threshold for forces, and 10^{-10} Hartree threshold for energy). Goedecker–Teter–Hutter pseudopotentials and the MOLOPT basis set were employed within the Gaussian and plane waves (GPW) formalism.

Supporting Information

Supporting Information is available from the Wiley Online Library or from the author.

Conflict of Interest

The authors declare no conflict of interest.

Data Availability Statement

The data that support the findings of this study are available from the corresponding author upon reasonable request.

Keywords

2D layered perovskites, organic cations, phonons, photoluminescence, Raman spectroscopy, self-trapped excitons, white light emission

[1] M. Yuan, L. N. Quan, R. Comin, G. Walters, R. Sabatini, O. Voznyy, S. Hoogland, Y. Zhao, E. M. Beauregard, P. Kanjanaboos, Z. Lu, D. H. Kim, E. H. Sargent, *Nat. Nanotechn.* **2016**, *11*, 872.

[2] B. Zhao, S. Bai, V. Kim, R. Lamboll, R. Shivanna, F. Auras, J. M. Richter, L. Yang, L. Dai, M. Alsari, X.-J. She, L. Liang, J. Zhang, S. Lilliu, P. Gao, H. J. Snaith, J. Wang, N. C. Greenham, R. H. Friend, D. Di, *Nat. Photonics* **2018**, *12*, 783.

[3] G. Grancini, M. K. Nazeeruddin, *Nat. Rev. Mater.* **2019**, *4*, 4.

[4] A. K. Jena, A. Kulkarni, T. Miyasaka, *Chem. Rev.* **2019**, *119*, 3036.

[5] C. Deng, G. Zhou, D. Chen, J. Zhao, Y. Wang, Q. Liu, *J. Phys. Chem. Lett.* **2020**, *11*, 2934.

[6] B. Febriansyah, T. Borzda, D. Cortecchia, S. Neutzner, G. Folpini, T. M. Koh, Y. Li, N. Mathews, A. Petrozza, J. England, *Angw. Chem., Int. Ed.* **2020**, *59*, 10791.

[7] X. Li, P. Guo, M. Kepenekian, I. Hadar, C. Katan, J. Even, C. C. Stoumpos, R. D. Schaller, M. G. Kanatzidis, *Chem. Mater.* **2019**, *31*, 3582.

[8] B. Dhanabalan, G. Biffi, A. Moliterni, V. Olieric, C. Giannini, G. Saleh, L. Ponet, M. Prato, M. Imran, L. Manna, R. Krahne, S. Artyukhin, M. P. Arciniegas, *Adv. Mater.* **2021**, *33*, 2008004.

[9] Y. Cho, T. C. Berkelbach, *J. Phys. Chem. Lett.* **2019**, *10*, 6189.

[10] M. D. Smith, A. Jaffe, E. R. Dohner, A. M. Lindenberg, H. I. Karunadasa, *Chem. Sci.* **2017**, *8*, 4497.

[11] M. D. Smith, H. I. Karunadasa, *Acc. Chem. Res.* **2018**, *51*, 619.

[12] M. D. Smith, B. A. Connor, H. I. Karunadasa, *Chem. Rev.* **2019**, *119*, 3104.

[13] J. Li, H. Wang, D. Li, *Front. Optoelectr.* **2020**, *13*, 225.

[14] E. R. Dohner, E. T. Hoke, H. I. Karunadasa, *J. Am. Chem. Soc.* **2014**, *136*, 1718.

[15] E. R. Dohner, A. Jaffe, L. R. Bradshaw, H. I. Karunadasa, *J. Am. Chem. Soc.* **2014**, *136*, 13154.

[16] A. Yangui, D. Garrot, J. S. Lauret, A. Lusson, G. Bouchez, E. Deleporte, S. Pillet, E. E. Bendeif, M. Castro, S. Triki, Y. Abid, K. Boukheddaden, *J. Phys. Chem. C* **2015**, *119*, 23638.

[17] X. Wang, W. Meng, W. Liao, J. Wang, R.-G. Xiong, Y. Yan, *J. Phys. Chem. Lett.* **2019**, *10*, 501.

[18] S. Li, J. Luo, J. Liu, J. Tang, *J. Phys. Chem. Lett.* **2019**, *10*, 1999.

[19] L. Zhang, Y. Hao, Y. Wu, W. Qin, X. Liu, B. Cui, S. Xie, *2D Mater.* **2020**, *7*, 035020.

[20] D. B. Straus, S. Hurtado Parra, N. Iotov, J. Gebhardt, A. M. Rappe, J. E. Subotnik, J. M. Kikkawa, C. R. Kagan, *J. Am. Chem. Soc.* **2016**, *138*, 13798.

[21] F. Thouin, A. R. Srimath Kandada, D. A. Valverde-Chávez, D. Cortecchia, I. Bargigia, A. Petrozza, X. Yang, E. R. Bittner, C. Silva, *Chem. Mater.* **2019**, *31*, 7085.

[22] T. Hu, M. D. Smith, E. R. Dohner, M.-J. Sher, X. Wu, M. T. Trinh, A. Fisher, J. Corbett, X. Y. Zhu, H. I. Karunadasa, A. M. Lindenberg, *J. Phys. Chem. Lett.* **2016**, *7*, 2258.

[23] W. Paritmongkol, E. R. Powers, N. S. Dahod, W. A. Tisdale, *J. Phys. Chem. Lett.* **2020**, *11*, 8565.

[24] Z.-G. Yu, *Phys. Chem. Chem. Phys.* **2019**, *21*, 22293.

[25] J. Luo, X. Wang, S. Li, J. Liu, Y. Guo, G. Niu, L. Yao, Y. Fu, L. Gao, Q. Dong, C. Zhao, M. Leng, F. Ma, W. Liang, L. Wang, S. Jin, J. Han, L. Zhang, J. Etheridge, J. Wang, Y. Yan, E. H. Sargent, J. Tang, *Nature* **2018**, *563*, 541.

[26] K. M. McCall, C. C. Stoumpos, S. S. Kostina, M. G. Kanatzidis, B. W. Wessels, *Chem. Mater.* **2017**, *29*, 4129.

[27] X. Gong, O. Voznyy, A. Jain, W. Liu, R. Sabatini, Z. Piontkowski, G. Walters, G. Bappi, S. Nokhrin, O. Bushuyev, M. Yuan, R. Comin, D. McCamant, S. O. Kelley, E. H. Sargent, *Nat. Mater.* **2018**, *17*, 550.

[28] F. Thouin, D. A. Valverde-Chávez, C. Quarti, D. Cortecchia, I. Bargigia, D. Beljonne, A. Petrozza, C. Silva, A. R. Srimath Kandada, *Nat. Mater.* **2019**, *18*, 349.

[29] B. Dhanabalan, Y.-C. Leng, G. Biffi, M.-L. Lin, P.-H. Tan, I. Infante, L. Manna, M. P. Arciniegas, R. Krahne, *ACS Nano* **2020**, *14*, 4689.

[30] C. M. Mauck, A. France-Lanord, A. C. Hernandez Oendra, N. S. Dahod, J. C. Grossman, W. A. Tisdale, *J. Phys. Chem. C* **2019**, *123*, 27904.

[31] N. S. Dahod, A. France-Lanord, W. Paritmongkol, J. C. Grossman, W. A. Tisdale, *J. Chem. Phys.* **2020**, *153*, 044710.

[32] B. A. Connor, L. Leppert, M. D. Smith, J. B. Neaton, H. I. Karunadasa, *J. Am. Chem. Soc.* **2018**, *140*, 5235.

[33] B. Martín-García, D. Spirito, G. Biffi, S. Artyukhin, B. Francesco, R. Krahne, *J. Phys. Chem. Lett.* **2021**, *12*, 280.

[34] P. Guo, C. C. Stoumpos, L. Mao, S. Sadasivam, J. B. Ketterson, P. Darancet, M. G. Kanatzidis, R. D. Schaller, *Nat. Commun.* **2018**, *9*, 2019.

[35] A. D. Christodoulides, P. Guo, L. Dai, J. M. Hoffman, X. Li, X. Zuo, D. Rosenmann, A. Brumberg, M. G. Kanatzidis, R. D. Schaller, J. A. Malen, *ACS Nano* **2021**, *15*, 4165.

[36] X. Li, J. M. Hoffman, M. G. Kanatzidis, *Chem. Rev.* **2021**, *121*, 2230.

[37] D. B. Straus, S. Hurtado Parra, N. Iotov, Q. Zhao, M. R. Gau, P. J. Carroll, J. M. Kikkawa, C. R. Kagan, *ACS Nano* **2020**, *14*, 3621.

[38] D. Cortecchia, J. Yin, A. Petrozza, C. Soci, *J. Mater. Chem. C* **2019**, *7*, 4956.

[39] B. Dhanabalan, A. Castelli, M. Palei, D. Spirito, L. Manna, R. Krahne, M. Arciniegas, *Nanoscale* **2019**, *11*, 8334.

[40] K. Momma, F. Izumi, *J. Appl. Crystallograph.* **2008**, *41*, 653.

[41] A. Lemmerer, D. G. Billing, *Dalton Trans.* **2012**, *41*, 1146.

[42] X.-L. Liu, X. Zhang, M.-L. Lin, P.-H. Tan, *Chin. Phys. B* **2017**, *26*, 067802.

[43] S. M. Rytov, *Sov. Phys. – Acoust.* **1956**, *2*, 68.

[44] E. M. Y. Lee, A. J. Mork, A. P. Willard, W. A. Tisdale, *J. Chem Phys.* **2017**, *147*, 044711.

[45] Q. Tu, I. Spanopoulos, E. S. Vasileiadou, X. Li, M. G. Kanatzidis, G. S. Shekhawat, V. P. Dravid, *ACS Appl. Mater. Interfaces* **2020**, *12*, 20440.

[46] M. A. Pérez-Osorio, Q. Lin, R. T. Phillips, R. L. Milot, L. M. Herz, M. B. Johnston, F. Giustino, *J. Phys. Chem. C* **2018**, *122*, 21703.

[47] M. A. Pérez-Osorio, R. L. Milot, M. R. Filip, J. B. Patel, L. M. Herz, M. B. Johnston, F. Giustino, *J. Phys. Chem. C* **2015**, *119*, 25703.

[48] B. Cheng, T.-Y. Li, P. Maity, P.-C. Wei, D. Nordlund, K.-T. Ho, D.-H. Lien, C.-H. Lin, R.-Z. Liang, X. Miao, *Commun. Phys.* **2018**, *1*, 80.

[49] W. Stadler, D. M. Hofmann, H. C. Alt, T. Muschik, B. K. Meyer, E. Weigel, G. Müller-Vogt, M. Salk, E. Rupp, K. W. Benz, *Phys. Rev. B* **1995**, *51*, 10619.

[50] R. Gautier, F. Massuyeau, G. Galnon, M. Paris, *Adv. Mater.* **2019**, *31*, 1807383.

[51] J. Hutter, M. Iannuzzi, F. Schiffmann, J. VandeVondele, *WIREs: Comp. Mol. Sci.* **2014**, *4*, 15.